ECCOMAS Congress 2016
VII European Congress on Computational Methods in Applied Sciences and Engineering
M. Papadrakakis, V. Papadopoulos, G. Stefanou, V. Plevris (eds.)
Crete Island, Greece, 5–10 June 2016

UNCERTAINTY QUANTIFICATION IN NUMERICAL SIMULATIONS OF THE FLOW IN THORACIC AORTIC ANEURYSMS

Alessandro Boccadifuoco[1], Alessandro Mariotti[2], Simona Celi[3], Nicola Martini [3] and Maria Vittoria Salvetti[2]

[1]Scuola Superiore Sant'Anna
Piazza Martiri della Libertà 33, 56127 Pisa, Italia
e-mail: alessandro.boccadifuoco@sssup.it

[2] Dipartimento di Ingegneria Civile e Industriale, Università di Pisa
Via G. Caruso 8, 56122 Pisa, Italia
e-mail: alessandro.mariotti@for.unipi.it, mv.salvetti@ing.unipi.it

[3] Fondazione CNR - Regione Toscana G. Monasterio,
Via Aurelia Sud, 54100 Massa, Italia
e-mail: s.celi@gmail.com, nicola.martini@gmail.com

Keywords: Ascending thoracic aortic aneurysms, CFD simulations, uncertainty quantification, polynomial chaos.

Abstract. *Numerical simulations of the flow in thoracic aortic aneurysms are carried out by using the open-source tool SimVascular and considering patient-specific geometries, obtained through in-vivo imaging. One of the main issues in these simulations is the choice of suitable boundary conditions, modeling the organs and vessels not included in the computational domain. The current practice is to use outflow conditions based on proximal resistance, capacitance and distal resistance (three-element Windkessel model), whose values are tuned to obtain a physiological behavior of the patient pressure. However, it is not known a priori how this choice affects the results of the simulation. A quantification of the impact on the numerical simulation results of uncertainties in the values of the Windkessel model parameters is carried out by using the generalized Polynomial Chaos approach. Different patient-specific geometries are considered, characterized by a different size of the aneurysms, and the effect of wall compliance is also investigated. We analyze the impact of the uncertainties in the selected outflow parameters on the time-averaged wall shear stress and on the oscillatory shear index, which are commonly used as hemodynamic descriptors.*

1 INTRODUCTION

The Ascending Thoracic Aortic Aneurysm (ATAA) is a life-threatening cardiovascular disease with remarkable morbidity and mortality. It is defined as a permanent and localized dilatation of the aorta, resulting from an irreversible loss of structural integrity of the aortic wall ([1, 2]), triggered by genetic mutations and/or mechanobiological aspects. Conventionally, an increase in diameter greater than 50% may be considered as evidence of an aneurysm ([3]). At the state of the art, clinical decisions on treatment strategies are currently based on empiric criteria, like the aortic diameter value or its growth rate.

From a biomechanical point of view, the aneurysmatic pathology has been investigated considering the structural change of the artery wall and its effects on the wall stress distribution, as well as performing fluid dynamical analyses in order to obtain the distribution of the wall shear stress. Biomechanical studies (see e.g. [4]) demonstrated that the criterion most widely used to predict the pathological state of ascending thoracic aortic aneurysms, i.e. the maximum aortic diameter, fails to predict rupture or dissection, especially in case of small-sized ascending thoracic aortic aneurysms and this means that other predictors are needed to understand and estimate the state of the aneurysm. Indeed, ATAAs are characterized by the presence of a complex hemodynamics, which could contribute to the onset/progression of the disease.

Advances in medical images provide not only accurate morphological features but also the non-invasive quantification of blood flow. In this context, the Phase Contrast Magnetic Resonance (PC-MRI) technique has become the prevalent imaging technique for non-invasive and detailed information due to its good spatial resolution with respect to hemodynamic quantities and due to the possibility of acquiring time-dependent data sets of the three-directional components of the blood flow velocity ([5, 6]).

In this scenario, CFD-based techniques are being used to build complex computer representations of the cardiovascular system in health and disease. CFD modeling enables investigation of pressure and flow fields at a temporal and spatial resolution unachievable by any clinical methodology, therefore allowing to easily quantify variables and indicators difficult to be obtained from *in-vivo* measurements. The main difficulty is represented by the assumptions made in CFD models, concerning, for instance, boundary conditions or the modeling of wall compliance and wall properties, which may affect the accuracy of CFD predictions. Thus, the combination between CFD simulation techniques and *in-vivo* and ex-vivo measurements is a key ingredient to set up reliable predictive tools. For instance, phase velocity and anatomic data ([7]) from PC-MRI have been used to perform patient-specific computational hemodynamics in healthy ([8, 9]) and diseased subjects ([10, 11]), in order to provide evidence of a possible relation of local wall shear stress with disease ([12, 13]), but, despite all those investigations, reliable patient-specific models are usually not easy to be obtained.

As previously mentioned, the accuracy of CFD predictions depends on the adopted modeling, but also on the quality of input data. For CFD applications it is unclear how detailed the clinical data needs to be in terms of geometry (segmented from medical images) and parametrization (variability described by the model and the tuning of patient-specific boundary conditions). In the present work we want to determine the impact of the uncertainties in the input data. This will provide further understanding of the relative importance of physiological parameters, determining those which are most influential, and those which can be assumed or averaged. In particular, we focused on the choice of suitable boundary conditions, modeling the organs and vessels not included in the computational domain. The current practice is to use outflow conditions based on proximal resistance, capacitance and distal resistance (three-element Windkessel model), whose

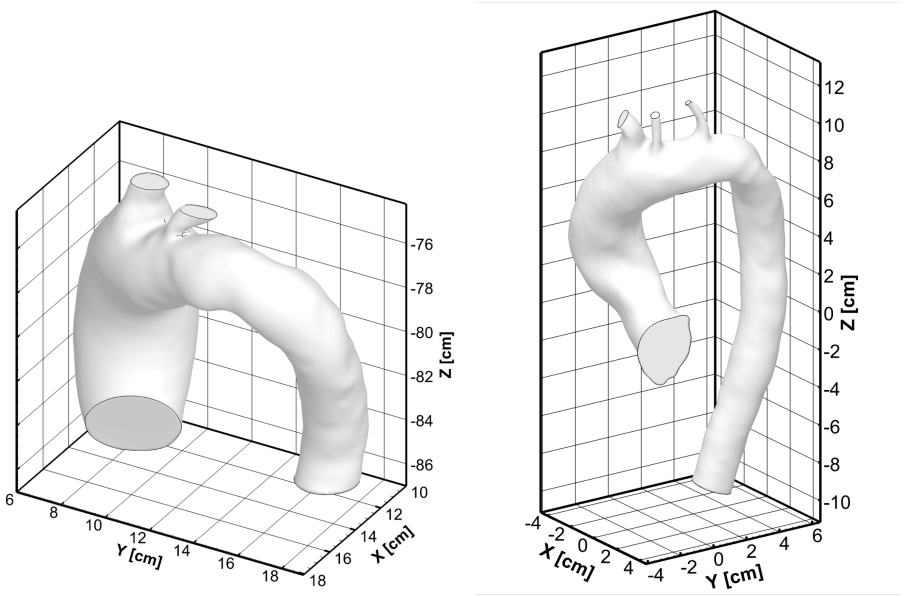

(a) Geometry A ($D_{r1} = 1.7$) (b) Geometry B ($D_{r2} = 1.5$)

Figure 1: Sketch of the considered geometries.

values are tuned to obtain a physiological behavior of the patient pressure. However, it is not known a priori how this choice affects the results of the simulation. Since a preliminary analysis showed that the proximal resistance and the capacitance are the main parameters affecting the pressure profile obtained in the Windkessel model, these two quantities were selected as uncertain parameters for the uncertainty quantification analysis, while a fixed reference value of the distal resistance was maintained.

This sensitivity was carried out through a stochastic approach, i.e. by modeling the unknown parameters as input random variables with a given probability distribution and propagating the uncertainties through the computational model to statistically quantify their effect on the results. The stochastic quantification was carried out by using the generalized Polynomial Chaos approach. Different patient-specific geometries were considered, characterized by a different size of the aneurysms, and the effect of wall compliance was also investigated. The impact of the uncertainties in the selected outflow parameters was investigated on the different quantities of interest; in particular, we analyzed the stochastic mean and standard deviation of the time-averaged wall shear stress and oscillatory shear index.

2 DEFINITION OF THE PROBLEM

2.1 Geometry definition

Two patient-specific geometries of thoracic aortas subjected to aneurysm in their ascending region were considered. Both cases were acquired by means of *in-vivo* imaging. The geometry A was reconstructed from Computed Tomography (CT), the geometry B by using Magnetic Resonance Imaging (MRI).

The two geometries are sketched in Figure 1. They differ in the severity of the disease, property quantified by the maximum diameter ratio $D_r = D_{\max}/D_{\text{healthy}}$, where $D_{\max}$ is the maximum transverse diameter (thus, obtained in correspondence of the widest section of the aneurysm) and D_{healthy} is the diameter of the healthy segment (measured in the descending region of the aorta). The two considered cases are characterized by $D_{r1} = 1.7$ and $D_{r2} = 1.5$,

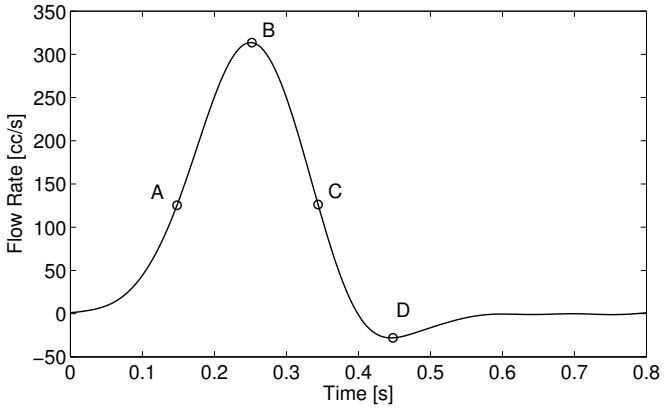

Figure 2: Flow rate profile imposed at the inlet section. The following characteristic time instants are highlighted: the maximum acceleration (A), the peak systole (B), the maximum deceleration (C) and early diastole (D).

respectively.

2.2 Simulation setup and numerical methodology

At the inlet section of the computational domain we imposed the physiological flow rate waveform of Figure 2 (see e.g. [14, 15]). The distribution of the velocity in the inlet section was assumed to be uniform.

The choice of outflow boundary conditions is more challenging, since they should accurately represent the effect of what happens outside the computational domain, modeling downstream organs and vessels (see e.g. [16] for a detailed overview). For this purpose, a three-element Windkessel model (also known as RCR model and sketched in Figure 3) was placed in correspondence of each outlet section, with a downstream pressure set to a constant reference value. Lumped parameter models are based on the analogy between electric circuits and hemodynamic problems: in particular, analogy is identified between the voltage difference and the drop in pressure, and between the current and the flow rate. In the presented scheme, the proximal and distal resistances (R_p and R_d) represent the viscous resistance the blood flow undergoes inside large and small vessels, respectively. The capacitance C quantifies the compliance, and thus the capability of storing fluid, of the major arteries. In the numerical deterministic computations used as a reference, these parameters were set in order to obtain a desired physiological behavior of the pressure profile ($125/80\,\mathrm{mmHg}$) in the simplified fully lumped model in which the contribution of the flow in the computational domain is not considered:

$$P(t) + R_d\, C \frac{dP(t)}{dt} = (R_p + R_d)Q(t) + R_p R_d\, C \frac{dQ(t)}{dt} \tag{1}$$

in which we imposed the inlet flow rate $Q(t)$ of Figure 2. Equation (1) was solved numerically. The resulting values are: $R_p = 106.5\,\mathrm{g\,cm^{-4}\,s^{-1}}$, $C = 10.4 \times 10^{-4}\,\mathrm{cm^4\,s^2\,g^{-1}}$ and $R_d = 1.67 \times 10^3\,\mathrm{g\,cm^{-4}\,s^{-1}}$.

Since descending from a fully lumped parameter model, the values of R_p, R_d and C were independent of the particular geometry considered. They were then distributed in the various

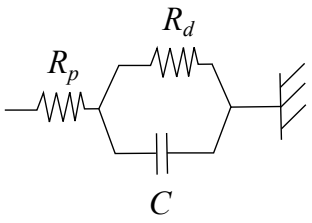

Figure 3: Scheme of a 3-Element Windkessel model.

Table 1: Summary of mechanical properties of the arterial wall used in the deformable simulations.

Quantity	Value
Density: ρ_{w} [$\mathrm{g\,cm^{-3}}$]	1.08
Young's Modulus: E_{w} [MPa]	3
Thickness: h_{w} [cm]	0.1
Poisson's Ratio: λ_{w}	0.499
Shear Correction Parameter: k_{w}	0.833

outlets as follows:

$$\begin{aligned} R_{p_i} &= R_p \frac{A_{\mathrm{tot}}}{A_i} \\ R_{d_i} &= R_d \frac{A_{\mathrm{tot}}}{A_i} \qquad \text{for } i = 1, \ldots, n_{\mathrm{outlets}} \\ C_i &= C \frac{A_i}{A_{\mathrm{tot}}} \end{aligned} \tag{2}$$

where n_{outlets} is the number of the outlets in the considered case (i.e., 3 in the first geometry and 4 in the second), A_i is the area of the outlet i and A_{tot} is the sum of the areas of all the outlets. The previous relations arise from the consideration that when increasing the vessel section the resistance opposed to the blood flow becomes smaller, while the wall compliance capability increases. Unlike R_p, R_d and C, the quantities obtained through Equation (2) are case-dependent.

On the arterial wall we imposed a no-slip condition. Both rigid and deformable simulations were performed. When considering the arterial wall compliance, for the sake of simplicity the aorta was assumed as an elastic, homogeneous and isotropic material, with a uniform wall thickness. The values of the mechanical properties chosen are reported in Table 1, where all dimensional properties, except for Young's Modulus, are expressed in *CGS* units.

The values of blood dynamic viscosity and density were specified as $\mu = 0.04\,\mathrm{g\,cm^{-1}\,s^{-1}}$ and $\rho = 1.06\,\mathrm{g\,cm^{-3}}$, respectively.

The hemodynamic simulations were performed with *SimVascular* (see [17]), an open-source comprehensive package specific for cardiovascular problems. The computational grid is unstructured and consists of tetrahedral elements, due to their adaptability to complex computational domains, like patient-specific geometries. The numerical code solves the three-dimensional incompressible Navier-Stokes equations by means of a stabilized finite element method, which makes it possible to choose linear shape functions for both velocity and pressure. For advancing in time, it uses the generalized α-method, which is an implicit technique that permits to achieve second order accuracy (see [18]).

The physical time step chosen for performing the numerical simulations was $0.001\,\mathrm{s}$ for both rigid and deformable cases, resulting in 800 time steps every cardiac cycle. After a grid sensitivity study, we chose a tetrahedral grid having approximately 2.2×10^5 for the geometry A and a tetrahedral grid with approximately 2.4×10^5 nodes for the geometry B.

Furthermore, each computation was run until the L_2 norms of the normalized differences between two successive pressure waveforms and between two successive flow rate waveforms were smaller than 10^{-5} (see [19]). These quantities were evaluated in correspondence of the descending aortic outlet section.

2.3 Quantities of interest and indicators

When considering the effects of the blood flow on the arterial wall, particular attention is given to the Wall Shear Stress (WSS), namely the modulus of the tangential stress $\boldsymbol{\tau}$ exerted by the flow on the arterial wall, i.e.

$$\mathrm{WSS}\left(\mathbf{x}, t\right) = \left|\boldsymbol{\tau}\left(\mathbf{x}, t\right)\right| \tag{3}$$

since it is thought to play an important role in the formation and growth of vascular diseases. Two additional parameters assume significant importance and are here used as hemodynamic descriptors: the Time-Averaged Wall Shear Stress (TAWSS), i.e. the wall shear stress throughout an entire cardiac cycle of period T, defined as:

$$\mathrm{TAWSS}\left(\mathbf{x}\right) = \frac{1}{T}\int_0^T \left|\boldsymbol{\tau}\left(\mathbf{x}, t\right)\right| \mathrm{d}t \tag{4}$$

and the Oscillatory Shear Index (OSI), which represents a measure of the deviation of the tangential stress from the predominant axial direction,

$$\mathrm{OSI}\left(\mathbf{x}\right) = \frac{1}{2}\left(1 - \frac{\left|\frac{1}{T}\int_0^T \boldsymbol{\tau}\left(\mathbf{x}, t\right) \mathrm{d}t\right|}{\frac{1}{T}\int_0^T \left|\boldsymbol{\tau}\left(\mathbf{x}, t\right)\right| \mathrm{d}t}\right) \tag{5}$$

This last indicator takes values in the range $[0, 0.5]$. Lower OSI values indicate that the tangential stresses at the wall are oriented predominately in the primary direction of the blood flow. On the other hand, high values indicate a very oscillatory behavior, 0.5 meaning that the instantaneous and the time-averaged vectors are never aligned.

3 RESULTS OF THE REFERENCE DETERMINISTIC SIMULATIONS

This section presents the results obtained for the reference deterministic simulations. For the geometry A (Figure 1(a)) simulations were carried out both for rigid and deformable walls, while for the geometry B (Figure 1(b)) only rigid walls were considered.

3.1 Geometry A with rigid walls

Figure 4 shows the instantaneous flow streamlines obtained in the simulation of the flow in the geometry A with rigid walls. The streamlines are colored according to the velocity magnitude. During systole they present a very regular behavior and the highest values of the velocity (Figure 4(a)), while recirculation areas occur in the diastolic phase (Figure 4(b)), which is characterized by reverse flow entering from the domain outlets.

In Figure 5 the WSS distributions at different time instants are shown. The four time instants marked in Figure 2 are considered. We selected the same WSS range in all the figures to highlight

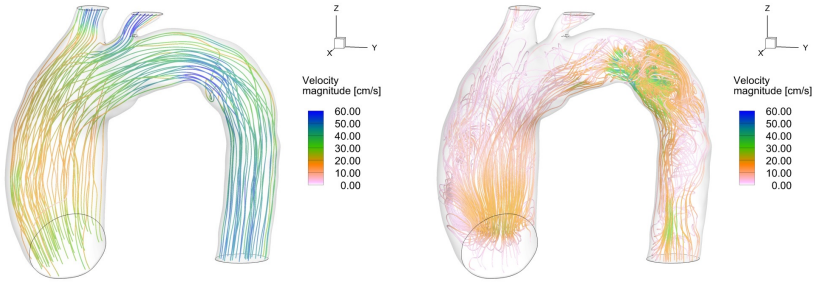

(a) Peak systole (b) Early diastole

Figure 4: Instantaneous flow streamlines for the geometry A with rigid walls. The streamlines are colored according to the velocity magnitude.

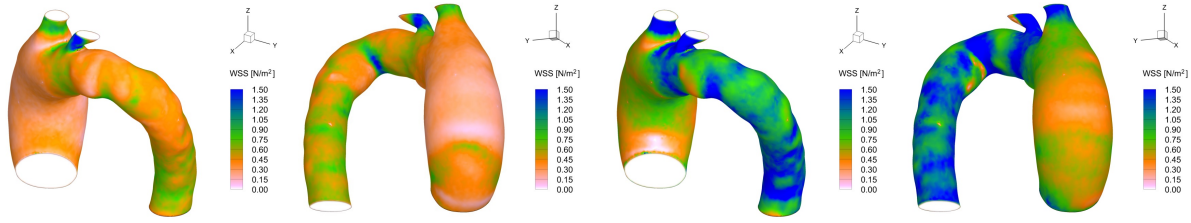

(a) Max acceleration (front) (b) Max acceleration (back) (c) Peak systole (front) (d) Peak systole (back)

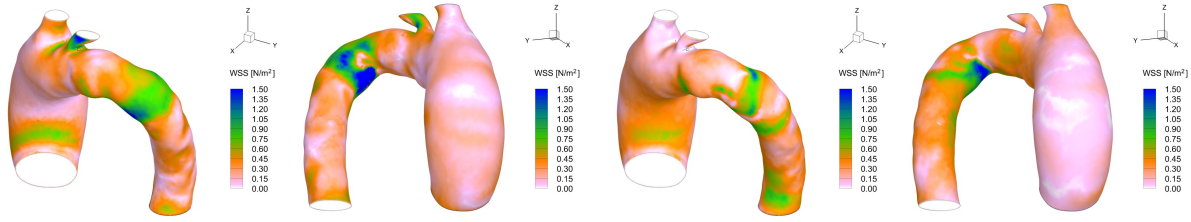

(e) Max deceleration (front) (f) Max deceleration (back) (g) Early diastole (front) (h) Early diastole (back)

Figure 5: WSS distribution for the geometry A with rigid walls.

the different magnitude of the tangential stresses along a cardiac cycle. The highest values of the stresses are found at peak systole in correspondence of the two small branches The stresses on the ascending region of the aorta are rather low during the whole cardiac cycle, possibly due to the large size of the aneurysm.

TAWSS and OSI are presented in Figures 6 and 7. The TAWSS distribution gives information on the mean behavior of WSS during the cardiac cycle, and it summarizes what found in the instantaneous maps: the most stressed regions are the areas with high curvature, while the aneurysm region is characterized by low stress. Since these mean stresses during a cardiac cycle are much smaller if compared with the maximum ones occurring during peak systole, a smaller TAWSS range was chosen.

High values of OSI (i.e., close to its maximum limit of 0.5) are associated to recirculation areas, see Figure 4(b) for comparison. Note that they occur also inside the aneurysm.

3.2 Effect of the wall compliance

In this section we evaluate the effect of the deformations of the arterial wall. The geometry A is considered.

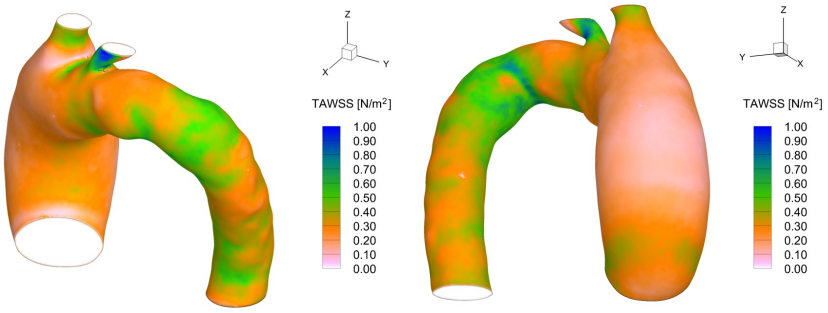

(a) Front view (b) Back view

Figure 6: TAWSS distribution for the geometry A with rigid walls.

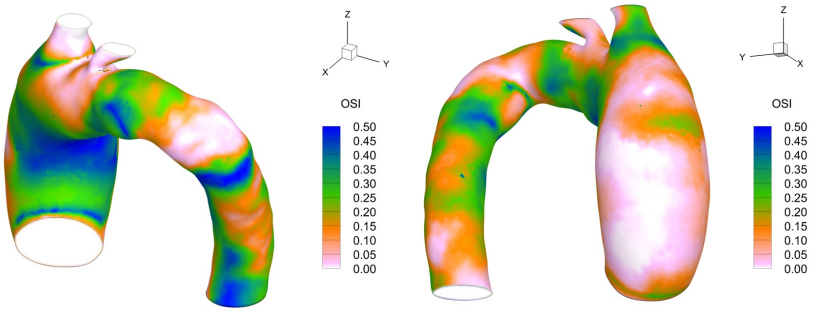

(a) Front view (b) Back view

Figure 7: OSI distribution for the geometry A with rigid walls.

The flow streamlines do not present significant differences if compared with the ones obtained with rigid walls, and thus they are not shown here. The only effect is a slight decrease of velocity magnitude, due to the widening of the vessel under the action of the blood flow.

The distributions of WSS and TAWSS are qualitatively very similar to the case of rigid walls, with only a variation in the quantitative values, which in the deformable case are lower (e.g., compare Figure 8 with Figure 6). This behavior could be expected given the possibility of the wall to move and relax.

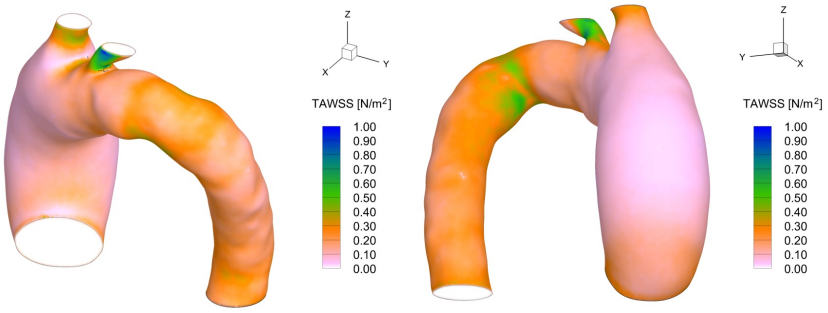

(a) Front view (b) Back view

Figure 8: TAWSS distribution for the geometry A with deformable walls.

The OSI distribution (Figure 9) does not present significant difference between deformable and rigid cases: this behavior is not surprising since this index is related to the velocity field,

which was found to be very similar in the two situations.

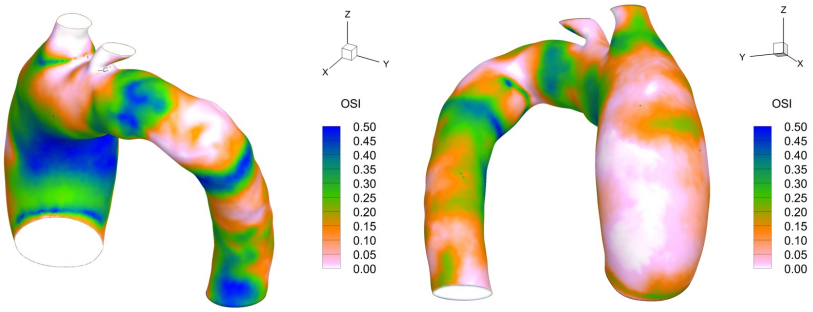

(a) Front view (b) Back view

Figure 9: OSI distribution for the geometry A with deformable walls.

3.3 Effect of the wall geometry

The effect of a different geometry and aneurysm size is evaluated by considering the geometry B (see Figure 1(b)). A simulation with rigid walls was performed with the same setup as for the geometry A.

Figure 10 shows the TAWSS distribution, and should be compared with Figure 6. The main effect of the geometry on TAWSS is the formation of areas of significant stress also in the ascending part of the aorta. This is due to the presence of a smaller aneurysm, and thus to the smaller size difference between the ascending and the descending regions.

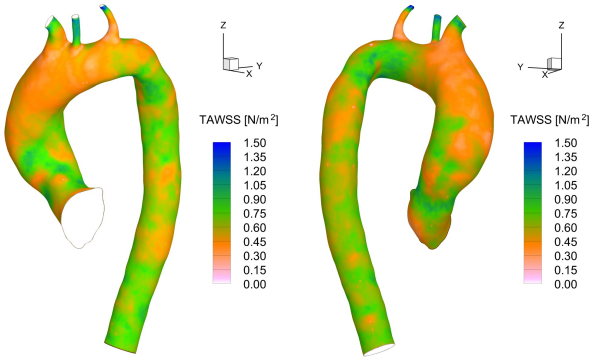

(a) Front view (b) Back view

Figure 10: TAWSS distribution for the geometry B with rigid walls.

High values of OSI can be found in the internal areas of both ascending and descending regions of the aorta, as shown in Figure 11, indicating thus that significant recirculation regions are present also inside the aneurysm.

4 UQ METHODOLOGY

The generalized Polynomial Chaos (gPC) approach, in its non-intrusive form, is an interpolant-type method, based on the projection of a given random process over an orthogonal known basis ([20]). The chaos expansion for a stochastic response output may be expressed as follows

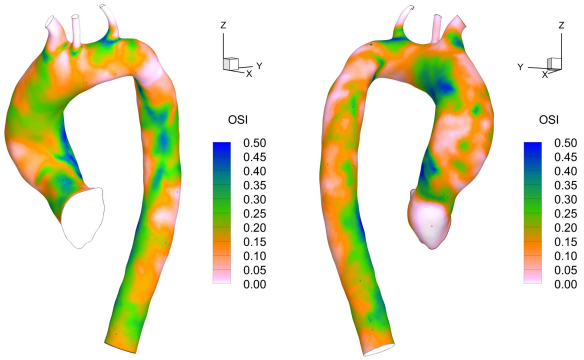

(a) Front view (b) Back view

Figure 11: OSI distribution for the geometry B with rigid walls.

(term-based indexing):

$$X(\omega) = \sum_{k=0}^{\infty} a_k \Phi_k(\boldsymbol{\xi}(\omega)) \tag{6}$$

where $X(\omega)$ is the random process, $\boldsymbol{\xi}(\omega)$ is the vector consisting of the independent random variables in the event space Ω, corresponding thus to the set of considered uncertain parameters, $\Phi_k(\boldsymbol{\xi})$ is the gPC polynomial of index k and a_k is the corresponding Galerkin projection coefficient.

The response surface is obtained by a truncation of the spectral decomposition (Equation (6)) to a finite limit T. Applying polynomial order bounds for all one-dimensional polynomials (tensor-product expansion), T is obtained as follows:

$$T = \prod_{i=1}^{M} (P_i + 1) - 1 \tag{7}$$

where M is the dimension of the random parameter space and P_i is the polynomial order bound for the i^{th} dimension.

Thanks to the orthogonality of the polynomial basis, the coefficient a_k can be computed as follows:

$$a_k = \frac{\langle X, \Phi_k \rangle}{\langle \Phi_k, \Phi_k \rangle} = \frac{1}{\langle \Phi_k, \Phi_k \rangle} \int_{\omega \epsilon \Omega} X \Phi_k \rho(\boldsymbol{\xi}) \, \mathrm{d}\xi \tag{8}$$

where $\rho(\boldsymbol{\xi})$ is the weight function associated with the chosen polynomial family. The integrals can be computed through different mathematical methods: Gaussian quadrature was used in the present work. The polynomial family to be used must be a priori specified. When dealing with Gaussian quadrature, an optimal family has a weight function similar to the probability measure, $W(\boldsymbol{\xi})$, of the random variables; it depends, thus, on the Probability Density Function (PDF) shape of the uncertain parameters.

As previously explained, the uncertain parameters in the Windkessel model are the proximal resistance, R_p, the capacitance, C, and the distal resistance, R_d. Since a UQ analysis with three uncertain parameters and 3D unsteady simulations is extremely expensive, a preliminary stochastic analysis was carried out to evaluate the single effect of R_p, C and R_d on the output pressure cycle in the 0D Windkessel model, i.e. neglecting the contribution of the 3D geometry of the aorta. This allowed to single out the effect of each uncertain parameter and, thus, to

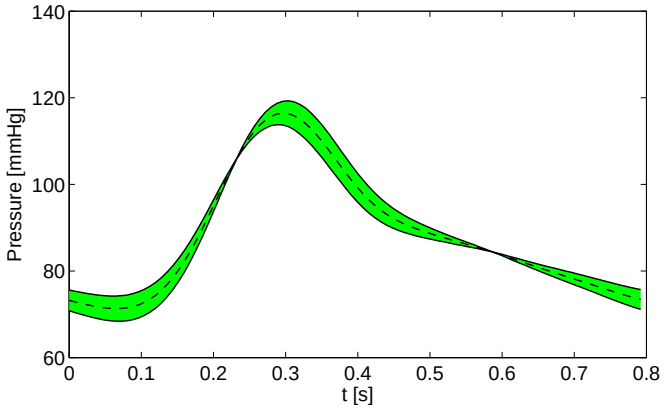

Figure 12: Effect of the variation of the capacitance C on the pressure waveform in correspondence of the descending aorta outlet section for the geometry A with rigid walls. The results are expressed in terms of stochastic mean (dashed line) $\pm$ stochastic standard deviation (continuous lines).

select the most important for the UQ analysis on 3D simulations, whose results are discussed in Sections 5 and 6.

After this 0D analysis, we selected R_p and C and allowed them to vary in the following ranges: $R_p \in [85.8, 148.4] \mathrm{g\,cm^{-4}\,s^{-1}}$ and $C \in [5.82 \times 10^{-4}, 12.6 \times 10^{-4}] \mathrm{cm^4\,s^2\,g^{-1}}$. First, we evaluated the effect of C alone: both rigid and deformable simulations were performed for the geometry A, while rigid walls were considered for the geometry B. Then, we investigated the combined effect of C and R_p: rigid simulations were performed for both the geometries.

The PDF of the input uncertain parameters is assumed to be uniform; this leads to the choice of Legendre polynomials for the gPC basis. The polynomial expansion is truncated to the third order for each dimension; hence, four quadrature points for each random variable are sufficient to compute the coefficients of the expansion. This leads to 4 or 16 hemodynamic simulations when considering one or two input parameters, respectively. These simulations were carried out for each quadrature point in the parameter space.

5 UQ ANALYSIS OF THE EFFECT OF UNCERTAINTIES IN THE VALUE OF C ON THE PRESSURE CYCLE AND ON THE FLOW FIELD

In this Section we evaluate how an uncertainty in the value of the capacitance C affects the quantities of interest reported in Section 2.3.

5.1 Geometry A with rigid walls

Figure 12 shows the output pressure waveform obtained in correspondence of the descending aorta outlet section. The results are presented in terms of the stochastic mean value $\pm$ the stochastic standard deviation. An increase of C leads to a reduction of the pulse pressure, as systolic and diastolic pressures become closer. On the other hand, the mean pressure P_{mean} is maintained practically constant.

The effect of the variation of C on TAWSS and OSI is evaluated in terms of the stochastic mean value and stochastic standard deviation, individually portrayed.

The stochastic mean distribution of TAWSS is almost equal to the reference deterministic result. The difference between the two TAWSS fields is shown in Figures 13(a) and 13(b) to allow a quantitative analysis. Differences are practically zero in most of the arterial lateral surface. Significant differences are found only in the upstream part of the descending aorta and

their absolute values are up to 10% of the corresponding stochastic mean values. In the same region we also find the largest stochastic variance of TAWSS (see Figures 13(c) and 13(d)). This means that this is the region in which TAWSS is most sensitive to the value of C.

Figures 14(a) and 14(b) report the difference between the stochastic mean distribution of OSI and the distribution obtained in the reference deterministic simulation. Again, differences are practically zero in the ascending aorta and in the two branches, independently of the value of OSI in those regions (note that in the reference deterministic simulation OSI assumes high values also in the internal part of the aneurysm, as shown in Figure 7(a)). On the other hand, significant positive and negative differences are found in localized regions of the aortic arch and of the descending aorta, where we also find the largest stochastic variance (see Figures 14(c) and 14(d)).

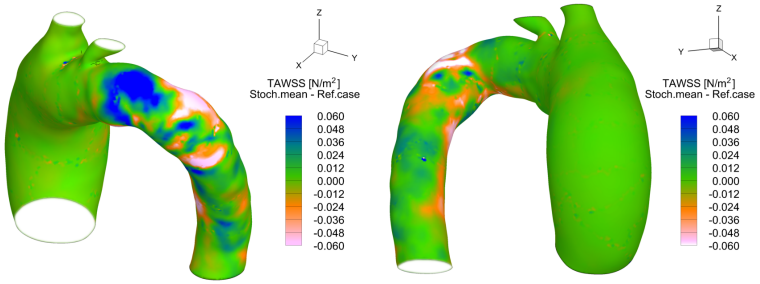

(a) Front view (b) Back view

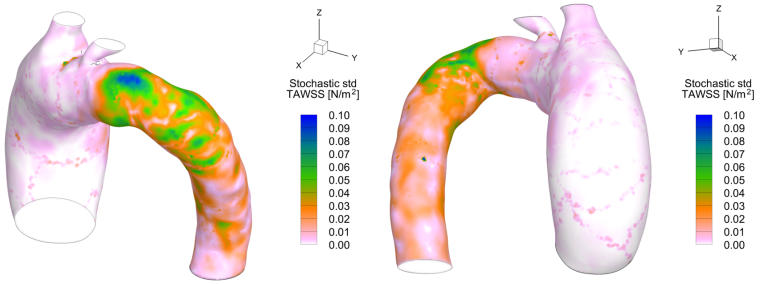

(c) Front view (d) Back view

Figure 13: Difference between the stochastic mean value and the reference deterministic value of TAWSS (a-b), and stochastic standard deviation of TAWSS (c-d) for the geometry A with rigid walls. Effect of uncertainties in the value of the capacitance C.

5.2 Effect of the wall compliance

In this Section we repeat the same UQ analysis as in Section 5.1 but considering the wall compliance. As before, the pressure waveform is evaluated in correspondence of the outlet section of the descending aorta, and the results are presented in terms of the stochastic mean value $\pm$ the stochastic standard deviation in Figure 15. The results obtained by considering the walls rigid are also reported in the same figure for comparison. It is clear that taking into account wall deformations leads to a smaller pulse pressure. This result could be expected, since the wall compliance acts as a further capacitance contribution and in both cases an increase of C reduces the difference between systolic and diastolic pressures, the mean pressure value being almost constant. The stochastic variance with C is also slightly reduced in the compliant case.

The indicators quantifying the stress levels on the arterial wall are again presented in terms of

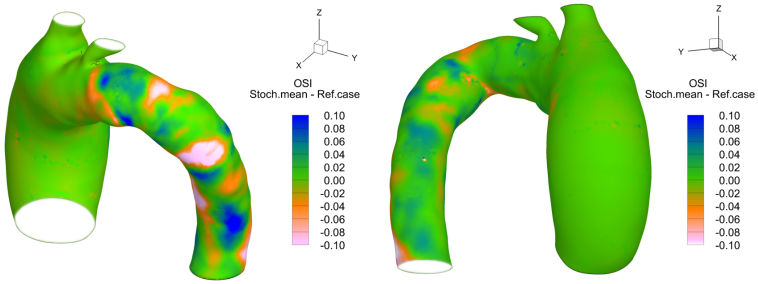

(a) Front view (b) Back view

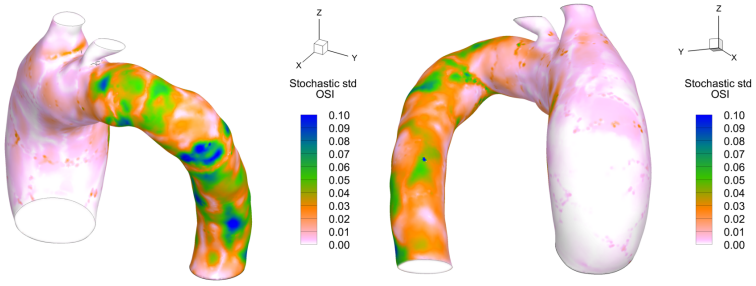

(c) Front view (d) Back view

Figure 14: Difference between the stochastic mean value and the reference deterministic value of OSI (a-b), and stochastic standard deviation of OSI (c-d) for the geometry A with rigid walls. Effect of uncertainties in the value of the capacitance C.

their stochastic mean value and of their stochastic standard deviation. As in the rigid case, for the sake of brevity we focus only on the cycle-averaged quantities.

Since the stochastic mean distribution of TAWSS is very close to the reference deterministic one, to allow a quantitative comparison in Figures 16(a) and 16(b) we present the difference between these two fields. As occurred in the rigid case, the differences are zero in most part of the aortic wall and are significant only in limited regions of the descending aorta. Their value never exceeds 10% of the corresponding stochastic mean. Figures 16(c) and 16(d) show the difference between the stochastic mean fields for deformable and rigid cases. This difference is uniform almost everywhere and negative in value, denoting that the arterial wall is subjected to smaller stresses when it has the possibility to expand and relax. However, the same qualitative behavior suggests that the flow topology does not significantly change.

The stochastic standard deviation of TAWSS is shown in Figures 16(e) and 16(f), while the difference between the deformable and the rigid cases is reported in Figures 16(g) and 16(h). The largest values of the stochastic standard deviation are found in the aortic arch and descending part (see Figures 16(e) and 16(f)) and they are smaller compared to the rigid case (see Figures 16(g) and 16(h)). As in the rigid case, the ascending region of the aorta presents no significant variability of the results.

Figures 17(a) and 17(b) show the difference between the stochastic mean distribution of OSI and the corresponding reference deterministic field. Again, most part of the aorta does not present significant differences. Differences can only be found in the distal aortic neck and in the descending region. However, they can reach about 30% of the corresponding stochastic mean value, thus being more important than the ones observed for TAWSS. Figures 17(c) and 17(d) highlight the difference between the OSI stochastic mean fields for deformable and rigid cases. Significant differences involve a larger portion of the aorta, mostly located at the aortic arch

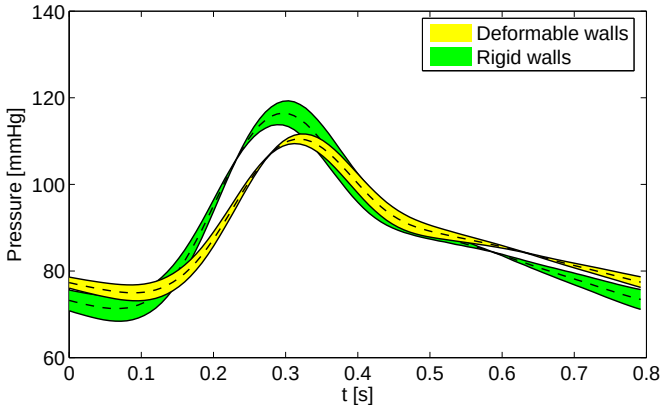

Figure 15: Effect of the variation of the capacitance C on the pressure waveform in correspondence of the descending aorta outlet section in the geometry A: comparison between deformable and rigid walls. The results are expressed in terms of stochastic mean (dashed line) $\pm$ stochastic standard deviation (continuous lines).

and descending part, but presenting some significant values also in the aneurysm region. This behavior can be related to the high sensitivity that OSI has to the flow field and to the locations of recirculation areas. A small variation in these locations can lead to a significant change in the OSI distribution. This can be deduced by analyzing the flow streamlines, here not shown for the sake of brevity.

Figures 17(e) and 17(f) show the stochastic standard deviation of OSI. Again, the descending aorta presents the largest variability, while the aneurysm region is characterized by small values of the stochastic variance. The comparison with the rigid case is evaluated in Figures 17(g) and 17(h), which illustrate the difference between the stochastic standard deviation of OSI for rigid and deformable walls. As observed for the stochastic mean distribution, the large differences in the descending aorta are possibly due to small changes in the flow field.

5.3 Effect of the wall geometry

In this Section we investigate the effect of the wall geometry by performing the UQ analysis on the geometry B with rigid walls. The output pressure waveform at the descending aorta outlet section is almost identical to the one obtained for geometry A with rigid walls (see Figure 12) and for sake of brevity is not shown.

The difference between the stochastic mean distribution of TAWSS and the corresponding reference deterministic distribution is presented in Figures 18(a) and 18(b). The effect of considering a smaller aneurysm is that the ascending and descending regions are closer in size. This produces a similar difference distribution in the whole aorta. These differences are not very high, except in some limited regions in which they reach 15% of the stochastic mean value at the same location.

Figures 18(c) and 18(d) show the stochastic standard deviation. Again, for the geometry B a significant variability is present also in the aneurysm region. The largest values of the stochastic standard deviation are about 25% of the corresponding stochastic mean value.

The difference between the stochastic mean value of OSI and the corresponding reference deterministic one is presented in Figures 19(a) and 19(b). Unlike what observed for the geometry A, differences affect not only the aortic arch and the descending aorta but also the aneurysm region. However, these differences may be again related to small changes in the flow field and small changes in location of recirculation areas.

Figures 19(c) and 19(d) illustrate the stochastic standard deviation obtained for OSI. High

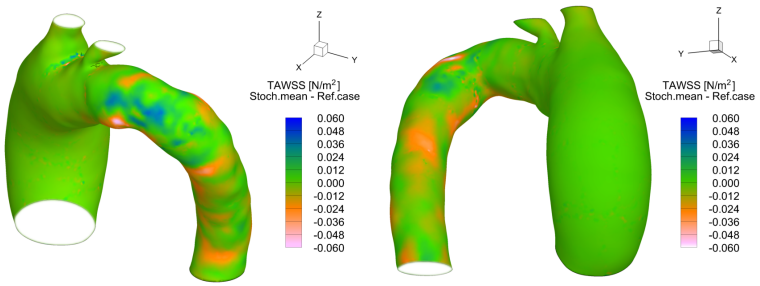

(a) Front view (b) Back view

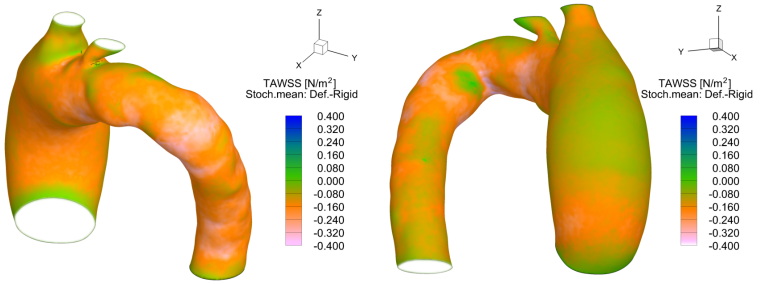

(c) Front view (d) Back view

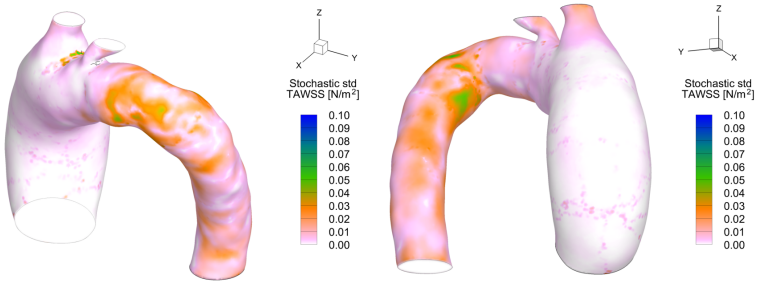

(e) Front view (f) Back view

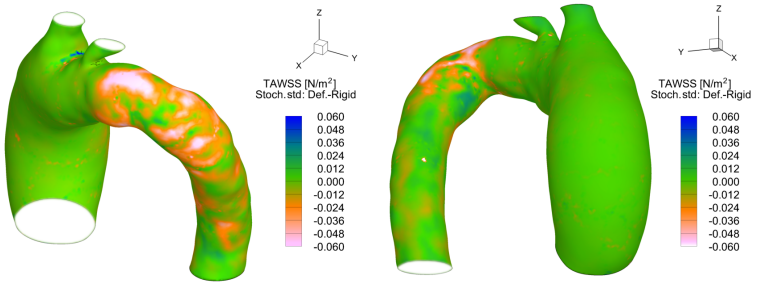

(g) Front view (h) Back view

Figure 16: Effect on the TAWSS distribution of uncertainties in the value of the capacitance C (geometry A with deformable walls): difference between the stochastic mean value and the reference deterministic value (a-b), difference between the stochastic mean values in deformable and rigid cases (c-d), stochastic standard deviation in the deformable case (e-f), and difference between the stochastic standard deviations in deformable and rigid cases (g-h).

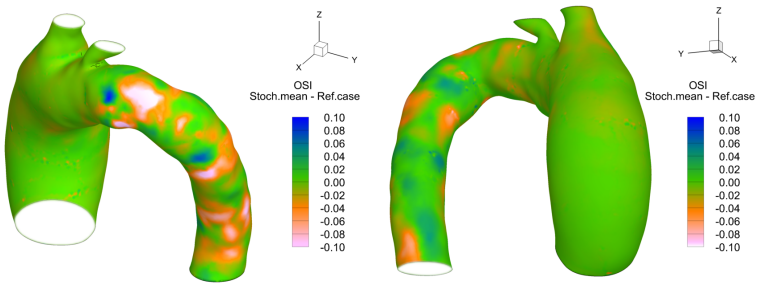

(a) Front view (b) Back view

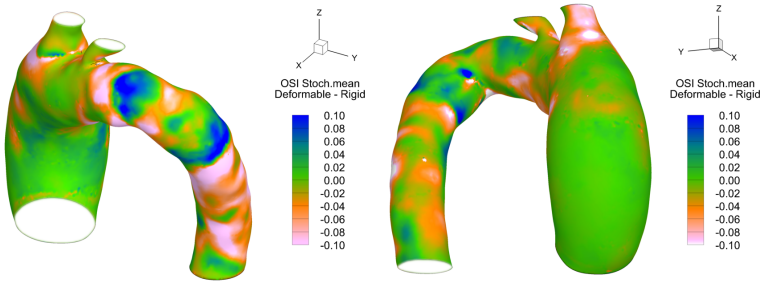

(c) Front view (d) Back view

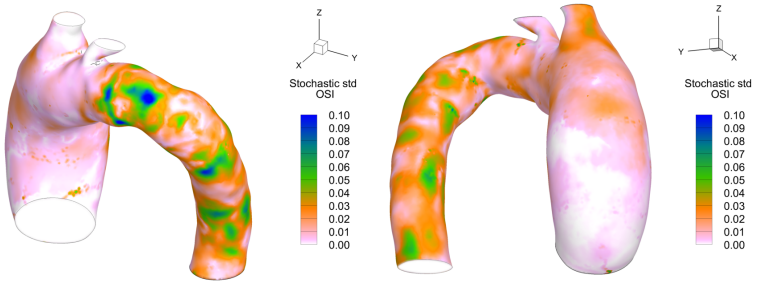

(e) Front view (f) Back view

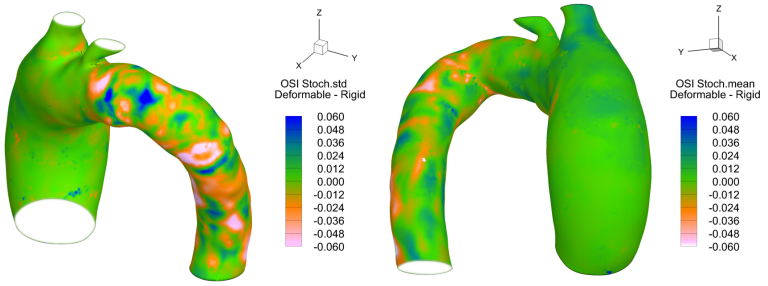

(g) Front view (h) Back view

Figure 17: Effect on the OSI distribution of uncertainties in the value of the capacitance C (geometry A with deformable walls): difference between the stochastic mean value and the reference deterministic value (a-b), difference between the stochastic mean values in deformable and rigid cases (c-d), stochastic standard deviation in the deformable case (e-f), and difference between the stochastic standard deviations in deformable and rigid cases (g-h).

variability is mostly found in the aneurysm region, where it can reach values about 35% of the stochastic mean value in the same location.

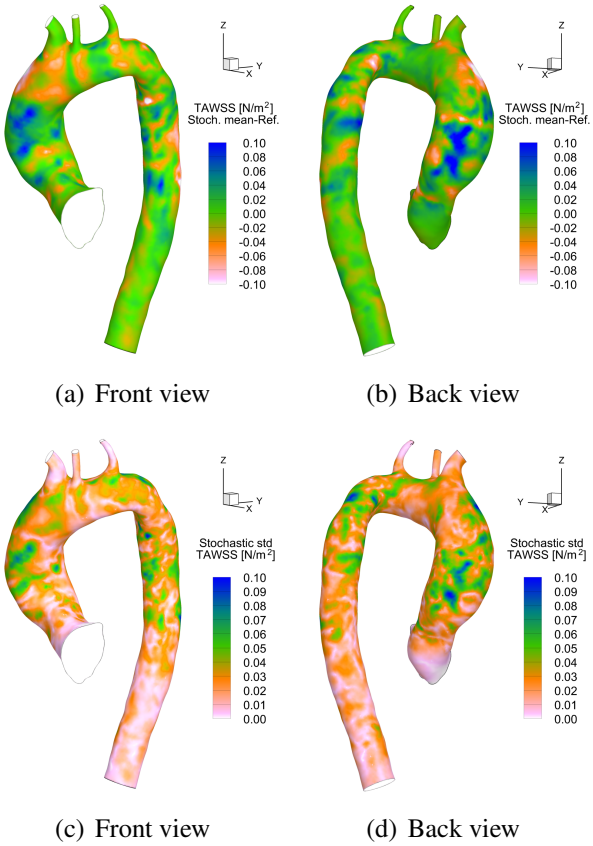

(a) Front view (b) Back view

(c) Front view (d) Back view

Figure 18: Difference between the stochastic mean value and the reference deterministic value of TAWSS (a-b), and stochastic standard deviation of TAWSS (c-d) for the geometry B with rigid walls. Effect of uncertainties in the value of the capacitance C.

6 UQ ANALYSIS OF THE EFFECT OF UNCERTAINTIES IN THE VALUES OF R_p AND C ON THE PRESSURE CYCLE AND ON THE FLOW FIELD

The aim of this Section is to assess the effect of uncertainties in the proximal resistance R_p and in the capacitance C on the quantities of interest reported in Section 2.3.

6.1 Geometry A with rigid walls

Figure 20(a) shows the output pressure waveform at the descending aorta outlet section, again in terms of the stochastic mean value $\pm$ the stochastic standard deviation. The main difference compared to the case in which only the capacitance C was allowed to vary is an increased variability of the results, especially in the region near the maximum pressure value (see Figure 12 for comparison). Figure 20(b) confirms this indication, illustrating the partial sensitivities to the two uncertain parameters alone and combined. For most part of the cardiac cycle the capacitance C is the main responsible of the variability of the results. In these regions the uncertainty in the proximal resistance R_p does not produce significant effects on the pressure profile, which thus maintains substantially the behavior of Figure 12. R_p becomes predominant in a small portion of the cycle, near peak systole. This explains why an increased stochastic standard deviation can be

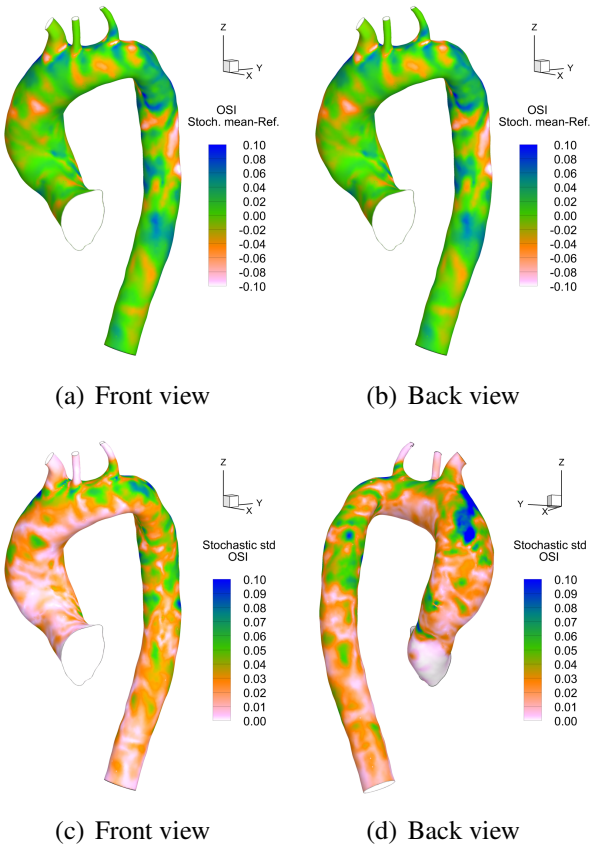

(a) Front view (b) Back view

(c) Front view (d) Back view

Figure 19: Difference between the stochastic mean value and the reference deterministic value of OSI, and stochastic standard deviation of OSI for the geometry B with rigid walls. Effect of uncertainties in the value of the capacitance C.

observed in the region near the maximum pressure value.

The effect of the second source of uncertainty (R_p) is evaluated considering the difference distributions between the stochastic outputs in the cases of two sources (C and R_p) and single source (C) of uncertainty. The averaged effect during a cardiac cycle of R_p on WSS is illustrated by the TAWSS distribution. Figures 21(a) and 21(b) show the difference distribution between the stochastic mean values of TAWSS in the two UQ analyses, while Figures 21(c) and 21(d) present the difference in the stochastic standard deviation. The effect of the second source of uncertainty on the stochastic mean value is very limited, with only small regions significantly affected. On the other side, its effect on the stochastic standard deviation is much more significant. The differences are mainly located in the region of the distal aortic neck and can reach 50% of the corresponding value obtained when considering only the variation of C.

Similar considerations apply also to OSI. The effect of considering R_p as an uncertain parameter has a limited effect on the stochastic mean value (see Figures 22(a) and 22(b)), while the stochastic standard deviation is in proportion much more affected (see Figures 22(c) and 22(d)). The difference respect to the case of single source of uncertainty is mainly located in the distal aortic neck. As found previously, this region presents again the highest sensitivity to the uncertain parameters.

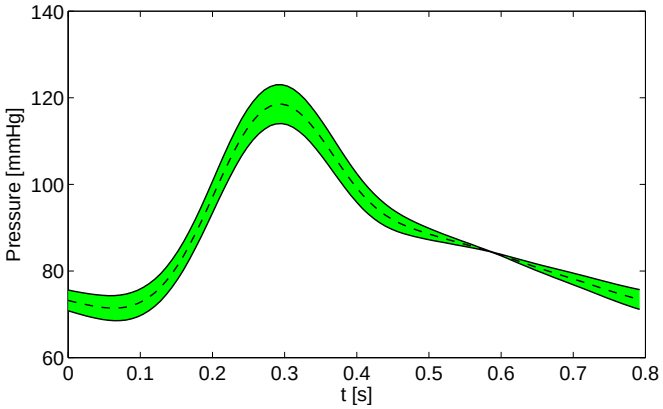

(a)

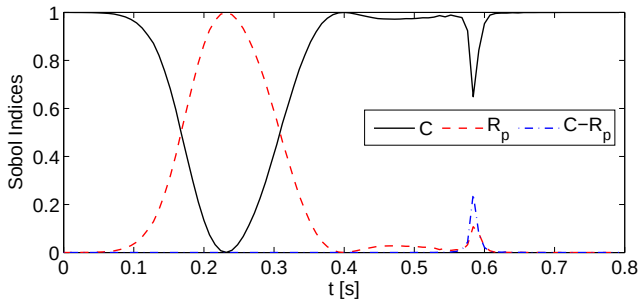

(b)

Figure 20: Effect of the variation of the capacitance C and proximal resistance R_p on the pressure profile in correspondence of the descending aorta outlet section (geometry A with rigid walls). The results are expressed in terms of stochastic mean $\pm$ stochastic standard deviation (a) and partial sensitivities to the two parameters (b).

6.2 Effect of the wall geometry

In this Section we investigate the effect of the geometry of the aorta. A UQ analysis with two uncertain parameters (C and R_p) was thus performed on the geometry B with rigid walls. The output pressure waveform at the descending aorta outlet section is almost identical to the one obtained for the geometry A (Figure 20) and for the sake of brevity is not shown here. This behavior suggests that the two geometries have basically the same resistance contribution on the flow, thus producing very small changes in the output pressure. This confirms what found in Section 5.3 for the case of only one source of uncertainty.

To isolate the effect of R_p on TAWSS and OSI, we again present for each stochastic output the difference field between the distribution obtained with two sources of uncertainty (C and R_p) and that obtained with a single source of uncertainty (C).

Figure 23 quantifies these differences for the stochastic mean value and stochastic standard deviation of TAWSS. As found for the geometry A, the second source of uncertainty R_p has a small effect on both the stochastic mean distribution (see Figures 23(a) and 23(b)) and the stochastic standard deviation (see Figures 23(c)), even if the variation of the stochastic standard deviation is in percentage terms again more significant. The effect of the geometry B is that these difference distributions are more uniform in the whole aorta, due to the similar size of the ascending and descending regions.

Considerations similar to those made for TAWSS also apply to OSI. Both the stochastic mean value (Figures 24(a) and 24(b)) and the stochastic standard deviation (Figures 24(c) and 24(d)) are little affected by the introduction of the second uncertain parameter R_p. However, 0.5 is the

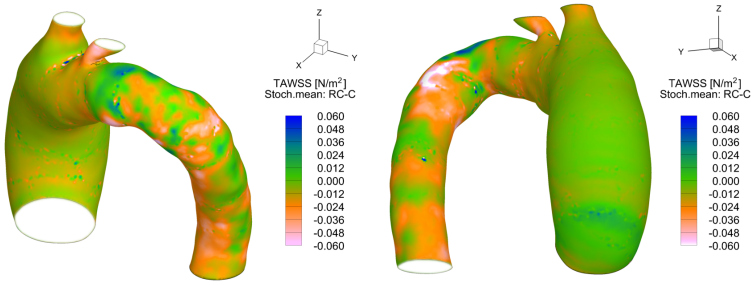

(a) Front view (b) Back view

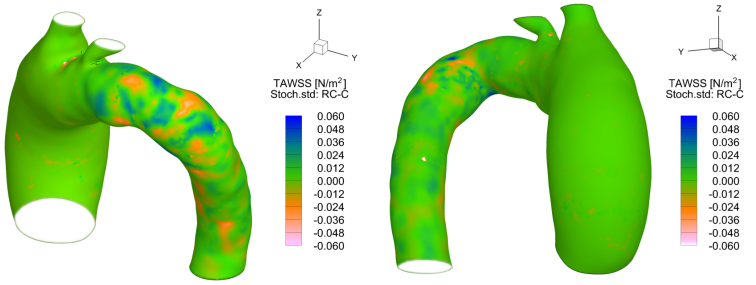

(c) Front view (d) Back view

Figure 21: Difference between the distributions of TAWSS obtained when considering both the uncertainties in C and R_p and the uncertainty in C alone. Stochastic mean (a-b) and stochastic standard deviation (c-d), geometry A with rigid walls.

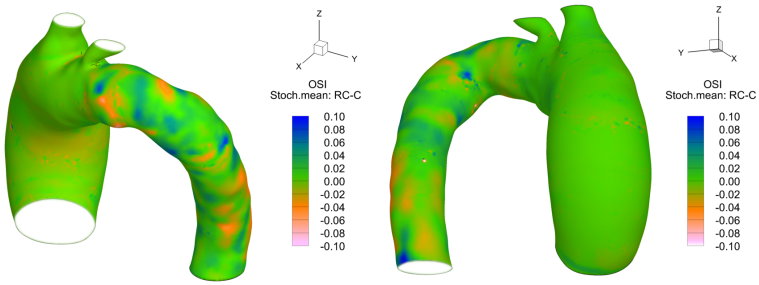

(a) Front view (b) Back view

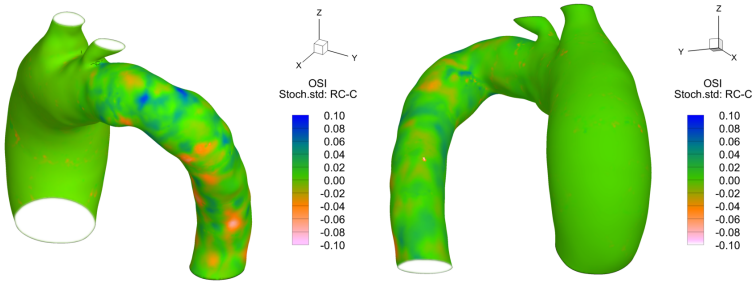

(c) Front view (d) Back view

Figure 22: Difference between the distributions of OSI obtained when considering both the uncertainties in C and R_p and the uncertainty in C alone. Stochastic mean (a-b) and stochastic standard deviation (c-d), geometry A with rigid walls.

maximum value that OSI can take, so even small differences in absolute terms can be relatively significant.

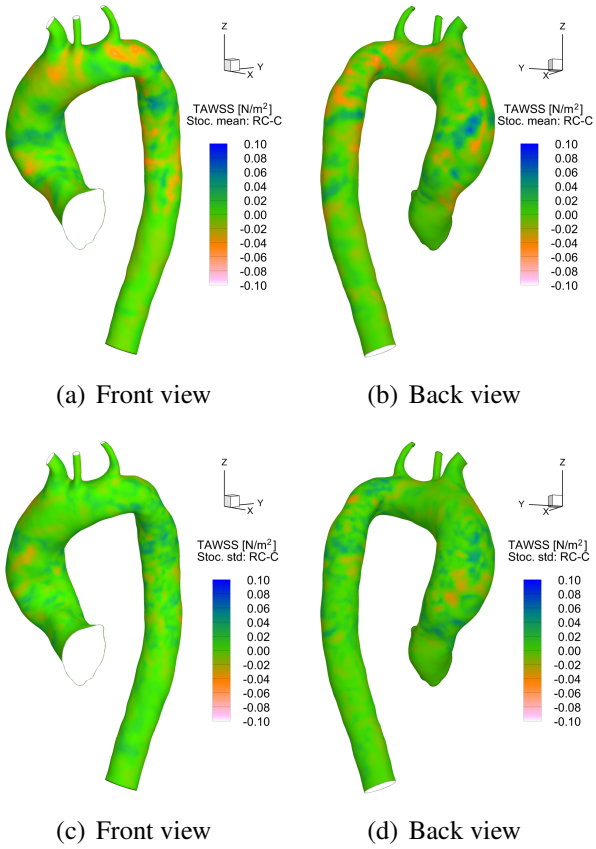

(a) Front view (b) Back view

(c) Front view (d) Back view

Figure 23: Difference between the distributions of TAWSS obtained when considering both the uncertainties in C and R_p and the uncertainty in C alone. Stochastic mean (a-b) and stochastic standard deviation (c-d), geometry B with rigid walls.

7 CONCLUDING REMARKS

The blood dynamics in two patient-specific ATAA geometries, characterized by different severity of the aneurysm pathology, was simulated. Deterministic simulations showed that the size of the aneurysm has a significant impact on the wall stress and flow feature, the smaller aneurysm being characterized by larger wall shear stresses and by a more recirculating flow. The wall compliance uniformly reduces the values of the shear stresses without changing their distribution, at least for the elastic, homogeneous, isotropic and constant thickness properties of the walls considered herein.

A stochastic sensitivity analysis to the uncertainties in the outflow boundary-condition parameters, namely the capacitance and the proximal resistance in the Winkdessel model, was also carried out. The mean stochastic values of TAWSS and OSI are very similar to those obtained in deterministic simulations carried out with values of the parameters guessed to obtain a desired physiological behavior of the pressure profile in a simplified fully lumped model. The stochastic variance of TAWSS and OSI was found to be very low inside the larger aneurysm, while more significant variations are present in localized regions of the aortic arch and of the descending aorta. For the geometry characterized by a smaller aneurysm, significant variability

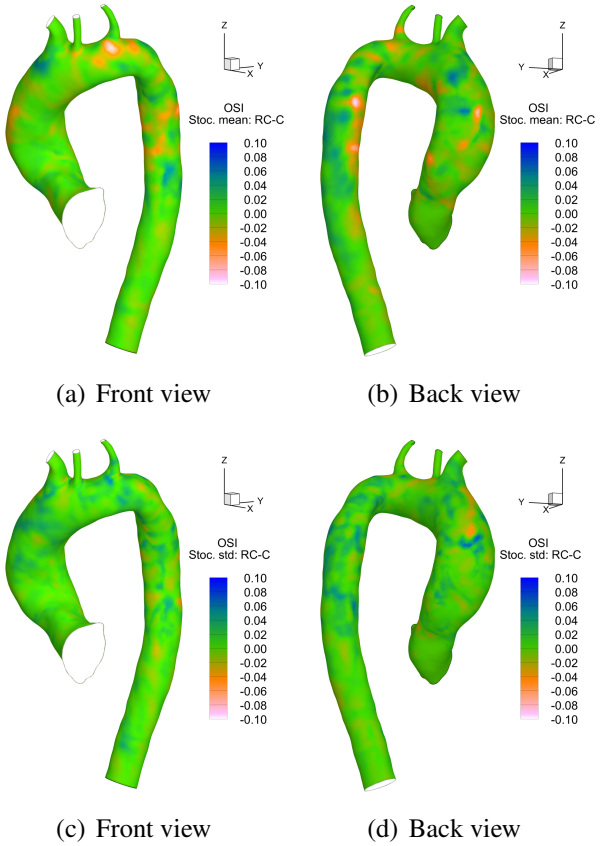

(a) Front view (b) Back view

(c) Front view (d) Back view

Figure 24: Difference between the distributions of OSI obtained when considering both the uncertainties in C and R_p and the uncertainty in C alone. Stochastic mean (a-b) and stochastic standard deviation (c-d), geometry B with rigid walls.

is present also inside the aneurysm, indicating that the stress numerical predictions inside small aneurysms are more sensitive to the outflow boundary conditions. The effects of wall compliance on the stochastic mean value of TAWSS are the same as those observed in the deterministic simulations, i.e. a uniform reduction of TAWSS. The variability of TAWSS with the considered boundary-condition parameters is also reduced in the case with compliant walls.

Finally, considering the uncertainties in the capacitance only and in both the capacitance and the proximal resistance leads to very similar distributions of the stochastic mean values of TAWSS and OSI for both geometries. This means that the effect of the proximal resistance on the stochastic mean distributions is very limited. Conversely, its effect on the stochastic variability of TAWSS and OSI is more significant, again for both considered geometries.

The proposed methodology permits to quantify the propagation of the uncertainties in input data on the output quantities of interest in patient-specific ATAA configurations. In the present case, we focused on uncertainties in the outflow parameters, but the same methodology could be applied to different types of uncertainties, as e.g. uncertainties in the geometry due to imaging/reconstruction errors or in the mechanical properties of the vessel walls. Finally, if *in-vivo* measured hemodynamic quantities are available, calibration of different simulation parameters could be carried out using a stochastic approach, providing thus a platform integrating CFD simulations and *in-vivo* measurements.

REFERENCES

[1] D. Botta and J.A. Elefteriades. Matrix metalloproteinases in thoracic aortic aneurysm disease. *International Journal of Angiology*, 15(1):1–8, 2006.

[2] J.S. Wilson and J.D. Humphrey. Evolving anisotropy and degree of elastolytic insult in abdominal aortic aneurysms: Potential clinical relevance? *Journal of Biomechanics*, 47(12):2995–3002, 2014.

[3] K.W. Johnston, R.B. Rutherford, M.D. Tilson, D.M. Shah, L. Hollier, and J.C. Stanley. Suggested standards for reporting on arterial aneurysms. *Journal of Vascular Surgery*, 13(3):452–458, 1991.

[4] S. Pasta, A. Rinaudo, A. Luca, M. Pilato, C. Scardulla, T.G. Gleason, and D.A. Vorp. Difference in hemodynamic and wall stress of ascending thoracic aortic aneurysms with bicuspid and tricuspid aortic valve. *Journal of Biomechanics*, 46(10):1729–1738, 2013.

[5] M. Markl, W. Wallis, and A. Harloff. Reproducibility of flow and wall shear stress analysis using flow-sensitive four-dimensional mri. *Journal of Magnetic Resonance Imaging*, 33(4):988–994, 2011.

[6] U. Morbiducci, R. Ponzini, G. Rizzo, M. Cadioli, A. Esposito, F.M. Montevecchi, and A. Redaelli. Mechanistic insight into the physiological relevance of helical blood flow in the human aorta: An in vivo study. *Biomechanics and Modeling in Mechanobiology*, 10(3):339–355, 2011.

[7] P. Volonghi, D. Tresoldi, M. Cadioli, A.M. Usuelli, R. Ponzini, U. Morbiducci, A. Esposito, and G. Rizzo. Automatic extraction of three-dimensional thoracic aorta geometric model from phase contrast mri for morphometric and hemodynamic characterization. *Magnetic Resonance in Medicine*, 2015.

[8] U. Morbiducci, R. Ponzini, D. Gallo, C. Bignardi, and G. Rizzo. Inflow boundary conditions for image-based computational hemodynamics: Impact of idealized versus measured velocity profiles in the human aorta. *Journal of Biomechanics*, 46(1):102–109, 2013.

[9] U. Morbiducci, D. Gallo, S. Cristofanelli, R. Ponzini, M.A. Deriu, G. Rizzo, and D.A. Steinman. A rational approach to defining principal axes of multidirectional wall shear stress in realistic vascular geometries, with application to the study of the influence of helical flow on wall shear stress directionality in aorta. *Journal of Biomechanics*, 48(6):899–906, 2015.

[10] S. Celi, F. Di Puccio, P. Forte, and L. Spadoni. Investigation on residual stress effects in fe simulations of balloon angioplasty. volume 2005, pages 249–250, 2005.

[11] S. Celi and S. Berti. Three-dimensional sensitivity assessment of thoracic aortic aneurysm wall stress: A probabilistic finite-element study. *European Journal of Cardio-thoracic Surgery*, 45(3):467–475, 2014.

[12] A. Frydrychowicz, A.F. Stalder, M.F. Russe, J. Bock, S. Bauer, A. Harloff, A. Berger, M. Langer, J. Hennig, and M. Markl. Three-dimensional analysis of segmental wall shear stress in the aorta by flow-sensitive four-dimensional-mri. *Journal of Magnetic Resonance Imaging*, 30(1):77–84, 2009.

[13] D.C. Wendell, M.M. Samyn, J.R. Cava, L.M. Ellwein, M.M. Krolikowski, K.L. Gandy, A.N. Pelech, S.C. Shadden, and J.F. LaDisa Jr. Including aortic valve morphology in computational fluid dynamics simulations: Initial findings and application to aortic coarctation. *Medical Engineering and Physics*, 35(6):723–735, 2013.

[14] D. Gallo, G. De Santis, F. Negri, D. Tresoldi, R. Ponzini, D. Massai, M.A. Deriu, P. Segers, B. Verhegghe, G. Rizzo, and U. Morbiducci. On the use of in vivo measured flow rates as boundary conditions for image-based hemodynamic models of the human aorta: Implications for indicators of abnormal flow. *Annals of Biomedical Engineering*, 40(3):729–741, 2012.

[15] J. Lantz, J. Renner, and M. Karlsson. Wall shear stress in a subject specific human aorta - influence of fluid-structure interaction. *International Journal of Applied Mechanics*, 3(4):759–778, 2011.

[16] A.D. Caballero and S. Laín. A review on computational fluid dynamics modelling in human thoracic aorta. *Cardiovascular Engineering and Technology*, 4(2):103–130, 2013.

[17] Alison Marsden and Shawn Shadden. SimVascular: Cardiovascular modeling and simulation. `http://simvascular.org`, 2015. Online; accessed 11-December-2015.

[18] Kenneth E. Jansen, Christian H. Whiting, and Gregory M. Hulbert. A generalized-α method for integrating the filtered Navier-Stokes equations with a stabilized finite element method. *Computer Methods in Applied Mechanics and Engineering*, 190(3-4):305 – 319, 2000.

[19] Lucian Itu, Puneet Sharma, Tiziano Passerini, Ali Kamen, Constantin Suciu, and Dorin Comaniciu. A parameter estimation framework for patient-specific hemodynamic computations. *Journal of Computational Physics*, 281(0):316 – 333, 2015.

[20] D. Xiu and G. Karniadakis. The Wiener-Askey polynomial chaos for stochastic differential equations. *SIAM Journal on Scientific Computing*, 24(2):619–644, 2003.